

## A self-adjoint velocity-stress full-waveform inversion approach to microseismic source estimation

Jordan Kaderli<sup>1</sup>, Matthew D. McChesney<sup>2</sup>, and Susan E. Minkoff<sup>1</sup>

### ABSTRACT

Accurate estimation of microseismic events in time and space enables important characterization of hydraulic fracture networks. Determining the orientation of the fracture can help differentiate between reactivation of an in situ fracture and a hydraulically induced fracture, which is important in characterizing the effectiveness of the stimulation process. We consider the source as separable in time and space and invert for a complete description of the source in one of these two dimensions assuming the other is known. We recover the wavelet, which includes the source amplitude and time evolution. In space, we recover a description of the source that is distributed and includes an estimate of the moment tensor at every point in the domain. A change of variables applied to the velocity-stress form of the elastic-wave equation ensures that the system is

self-adjoint. Thus, full-waveform inversion can be tailored to estimate microseismic events with limited modifications to the forward wave solver. The inversion does not use any a priori assumptions about the form of the source, does not require a good starting guess for accurate source recovery, and is robust in the presence of noise. Applying this technique to wavelet inversion correctly recovers a 30 Hz Ricker wavelet from a zero initial guess with and without noise. Furthermore, for a realistic microseismic event generated from coupled flow and deformation modeling, the algorithm recovers the peak time and approximate shape of the wavelet. In fact, our algorithm recovers as much of the true wavelet as possible given the energy in the observed data. Furthermore, experiments involving a distributed source in the shape of an ellipse illustrate that the inversion scheme can not only estimate the focal mechanism of failure events, but also the geometry of the failure plane.

### INTRODUCTION

The monitoring of microseismic events is a very active area of research with applications in fields such as mining, CO<sub>2</sub> sequestration, reservoir monitoring, and geothermal systems. Perhaps the most common use of microseismic monitoring is in the investigation of hydraulic fracture networks (Gharti et al., 2011; Maxwell, 2014; Eyre and van der Baan, 2015; Kamei et al., 2015; Maxwell et al., 2015). Hydraulic fracturing is used to extract oil and gas from low-permeability formations such as mudrocks. Fluid is injected into the rock at high pressure to create fractures through which oil and gas can flow more easily to the wellbore. The failure of the formation rock during injection can lead to the generation of microseismic events. Geoscientists and engineers use information about microseismic events to characterize the nature and extent of the hy-

draulic fracture network. Furthermore, determining the orientation of the fracture can help differentiate reactivation of an in situ fracture from a hydraulically induced fracture, which is important in characterizing the effectiveness of the stimulation process. Researchers have developed several techniques for estimating the locations, radiation patterns, and source time functions for such microseismic events. These methods include traditional techniques, such as P- and S-wave traveltimes (Rutledge and Phillips, 2003; Eisner et al., 2009) and traveltimes inversion (Oye and Roth, 2003), as well as migration-based methods (Artman et al., 2010; Gharti et al., 2011; Douma et al., 2013; Douma and Snieder, 2014; Zhebel and Eisner, 2015; Trojanowski and Eisner, 2017).

Full-waveform inversion (FWI), which has been widely used to image and quantify the subsurface (Virieux and Operto, 2009;

Manuscript received by the Editor 20 August 2017; revised manuscript received 16 February 2018; published ahead of production 09 June 2018; published online 2 August 2018.

<sup>1</sup>The University of Texas at Dallas, Department of Mathematical Sciences, 800 West Campbell Road, Richardson, Texas 75080, USA. E-mail: jxk124230@utdallas.edu; sminkoff@utdallas.edu.

<sup>2</sup>The University of Texas at Dallas, Department of Geosciences, 800 West Campbell Road, Richardson, Texas 75080, USA. E-mail: mdm075000@utdallas.edu.

© 2018 Society of Exploration Geophysicists. All rights reserved.

Fichtner, 2011; Métivier et al., 2017), has also been used to estimate the source of a seismic event (Wu and McMechan, 1996; Minkoff and Symes, 1997; Ramos-Martinez and McMechan, 2001; Vavryčuk and Kühn, 2012; Sjögren and Petersson, 2014). More recently, researchers have used FWI for microseismic source estimation. For example, Jarillo Michel and Tsvankin (2014a, 2014b), Kim et al. (2011), and Morency and Mellors (2012) use FWI to invert for the source location  $\mathbf{x}_s$  and moment tensor, but they require a very good initial estimate of the source for the inversion algorithm to succeed. Similarly, Zhang et al. (2014) use the displacement form of the elastic-wave equation to invert for the source location and source focal mechanism in space. They admit, however, that their inversion results are often “entirely different from the true parameters” (Zhang et al., 2014). In the case of acoustics, Kaderli et al. (2015) as well as Kamei and Lumley (2014) and Sharan et al. (2016) assume that the source term of the wave equation can be separated into a product of two functions: a spatial component that depends only on position and a temporal component that depends only on time (e.g.,  $s(\mathbf{x}, t) = f(\mathbf{x})w(t)$ ). Kaderli et al. (2015) introduce the idea of considering the entire domain as a potential source function in which each point of the domain is assigned a value indicating the magnitude of deformation of the medium. The temporal component shows the evolution of this deformation through time. This approach does not require the source to be a point source (a typical simplifying assumption that is not physically realistic in the case of a rupturing fault). In fact, no a priori assumptions are made regarding the extent or distribution of the spatial or temporal components of the source. In this paper, we extend this idea to the case of elastic wave propagation, and we will apply the methodology to realistic rupture behaviors as modeled by flow and deformation simulations. Specifically, we determine the entire source description for the time-domain wavelet (including time evolution and amplitude) or the entire spatial description (the distribution of source events in space and the moment tensor components at each point in the domain). Additional advantages of this approach include accurate results in the presence of noise and in the absence of a good initial estimate of the source.

The velocity-stress formulation of the elastic-wave equation is desirable for microseismic source estimation in which the recorded wavefields are often velocities (geophone data). And while the displacement form of the elastic-wave equation has the advantage of being self-adjoint, there are simulation advantages of the velocity-stress formulation as well. Yao and Margrave (2000) note that when the velocity-stress formulation is solved using staggered-grid finite differences, the entire solution does not need to be stored in memory, and one can easily extend the solution technique to higher order difference operators. Furthermore, the algorithm can be easily implemented on scalar, vector, or parallel computers. Classic papers on the velocity-stress formulation include those by Madariaga (1976), Virieux (1984, 1986), and Levander (1988). Borisov and Singh (2015) and Vigh et al. (2014) use the velocity-stress formulation to invert for the wave velocities, and Baumstein et al. (2009) and Wang et al. (2012) use dimensional analysis to further study the properties of the gradient needed for velocity inversion. Recently, Gao et al. (2017) use FWI via the velocity-stress formulation in two dimensions to estimate the source location and origin time simultaneously. They use a group sparsity constraint that helps to focus the source in space. However, they do not invert for the moment tensor. Castellanos et al. (2011) apply a useful change of variables

to the velocity-stress equations to invert for the mechanical earth parameters using a self-adjoint operator. However, they did not discuss source inversion. Fabien-Ouellet et al. (2016, 2017) develop a change of variables that is similar to that used by Castellanos et al. (2011) to invert for P- and S-wave velocities and the Q-factor. In this paper, we extend the work of Castellanos et al. (2011) to invert for the spatial and temporal components of a microseismic source via the velocity-stress formulation and a self-adjoint operator.

Because researchers commonly use gradient-based optimization to minimize the objective functional, we begin by discussing the computation of the gradient for the space and time components of the source. We then demonstrate the effectiveness of this methodology by using this gradient in several synthetic numerical inversion experiments. Specifically, we invert for the temporal component of the source, assuming a point source in space with a known moment tensor. We also include experiments to estimate much more difficult and realistic microseismic sources generated from flow and deformation modeling of a single fracture. We consider a point source in space and a distributed elliptical source, which is a more realistic description of a rupture on a fault. In summary, our work differs substantially from the previous work in that

- 1) We apply a change of variables to the velocity-stress form of the elastic-wave equation, which allows us to estimate the microseismic source via an efficient self-adjoint operator. Hence, one can reuse the forward code for the adjoint solve. We calculate the gradient for the time and space components of the source in this case.
- 2) We consider the source as being separable in time and space, and we invert for a complete description of the source in one of these two dimensions assuming the other is known. In time, we recover the wavelet, which includes the source amplitude and time evolution. In space, we recover a description of the source that is distributed in space and includes an estimate of the moment tensor at every point in the domain.
- 3) We apply this methodology to realistic microseismic event experiments generated by coupled fracture mechanics and fluid flow.

In this work, we do not address the more complex joint inversion problem for simultaneous estimation of the temporal and spatial source components. We also do not investigate regularization that would help focus the source in space and is necessary for joint inversion.

## THEORY

We use FWI to estimate the source of a microseismic event by minimizing the misfit between the recorded and predicted data via a gradient-based optimization algorithm. We begin by discussing the change of variables given by Castellanos et al. (2011), which produces a self-adjoint system for the adjoint state method (Gunzburger, 2003; Oberai et al., 2003; Plessix, 2006; Fichtner, 2011). We then use this modified system to compute the gradient with respect to the source components (spatial and temporal).

### Forward problem

We model wave propagation through a 3D isotropic elastic medium using the velocity-stress formulation of the wave equation (Sleefe et al., 1998; Minkoff, 2002):

$$\begin{aligned}\frac{\partial v_i(\mathbf{x}, t)}{\partial t} &= \frac{1}{\rho(\mathbf{x})} \frac{\partial \sigma_{ij}(\mathbf{x}, t)}{\partial x_j} + \frac{1}{\rho(\mathbf{x})} \left[ f_i(\mathbf{x}, t) + \frac{\partial m_{ij}^a(\mathbf{x}, t)}{\partial x_j} \right], \\ \frac{\partial \sigma_{ij}(\mathbf{x}, t)}{\partial t} &= \lambda(\mathbf{x}) \frac{\partial v_k(\mathbf{x}, t)}{\partial x_k} \delta_{ij} + \mu(\mathbf{x}) \left[ \frac{\partial v_i(\mathbf{x}, t)}{\partial x_j} + \frac{\partial v_j(\mathbf{x}, t)}{\partial x_i} \right] \\ &\quad + \frac{\partial m_{ij}^s(\mathbf{x}, t)}{\partial t}.\end{aligned}\quad (1)$$

Here,  $\mathbf{x}$  is the spatial position,  $t$  is the time,  $v_i$  are the particle velocity vector components,  $\sigma_{ij}$  are the stress tensor components,  $\rho$  is the mass density,  $\lambda$  and  $\mu$  are the Lamé parameters,  $\delta_{ij}$  is the Kronecker delta,  $f_i$  are the force source components, and  $m_{ij}^s$  and  $m_{ij}^a$  are the symmetric and antisymmetric parts of the moment density tensor, respectively. Due to our assumption of linear elasticity, we focus in this work on the symmetric part of the moment density tensor. The above system consists of nine equations, three for the particle velocity and six for the stress tensor. We assume that the source can be separated into a temporal component (a wavelet  $w(t)$ ), which depends only on time and a spatial component (either in the form of a moment tensor source  $m_{ij}(\mathbf{x})$  or a directed force  $f_i(\mathbf{x})$ ), which is a function of position only.

For a symmetric moment tensor source, equation 1 in vector form becomes

$$\frac{\partial \mathbf{u}}{\partial t} = \mathbf{A}\mathbf{u} + \mathbf{s} \frac{dw}{dt}, \quad (2)$$

where the solution vector

$$\mathbf{u} = (v_1, v_2, v_3, \sigma_{11}, \sigma_{22}, \sigma_{33}, \sigma_{12}, \sigma_{13}, \sigma_{23})^T, \quad (3)$$

the source vector

$$\mathbf{s} = (0, 0, 0, m_{11}, m_{22}, m_{33}, m_{12}, m_{13}, m_{23})^T, \quad (4)$$

and the differential operator matrix  $\mathbf{A}$  is given in equation 1.

Following Castellanos et al. (2011), we apply a suitable change of variables to equation 1, which produces a self-adjoint system. *Thus, we will be able to reuse the forward wave solver when solving the adjoint equations.* The transformed system is

$$\Lambda \frac{\partial \mathbf{u}'}{\partial t} = \mathbf{A}' \mathbf{u}' + \mathbf{s}' \frac{dw}{dt}, \quad (5)$$

where

$$\mathbf{s}' = \Lambda \mathbf{T} \mathbf{s} \quad \text{and} \quad \mathbf{A}' = \Lambda \mathbf{T} \mathbf{A} \mathbf{T}^{-1}. \quad (6)$$

Here,  $\Lambda$  is the  $9 \times 9$  diagonal matrix such that

$$\text{diag}(\Lambda) = \left( \rho, \rho, \rho, \frac{1}{3\lambda + 2\mu}, \frac{1}{2\mu}, \frac{1}{2\mu}, \frac{1}{2\mu}, \frac{1}{2\mu}, \frac{1}{2\mu} \right). \quad (7)$$

In addition,  $\mathbf{u}'$  is the transformed solution vector and  $\mathbf{T}$  is the linear transformation such that

$$\mathbf{u}' = \mathbf{T} \mathbf{u}, \quad (8)$$

where

$$\mathbf{u}' = \left( v_1, v_2, v_3, \frac{1}{\sqrt{3}}(\sigma_{11} + \sigma_{22} + \sigma_{33}), -\frac{1}{\sqrt{6}}(\sigma_{11} + \sigma_{22} - 2\sigma_{33}), -\frac{1}{\sqrt{2}}(\sigma_{11} - \sigma_{22}), \sqrt{2}\sigma_{12}, \sqrt{2}\sigma_{13}, \sqrt{2}\sigma_{23} \right)^T. \quad (9)$$

An important result of this transformation is that  $\mathbf{A}'$  is now independent of  $\rho$ ,  $\lambda$ , and  $\mu$ . Explicit descriptions of matrices  $\mathbf{A}$ ,  $\mathbf{A}'$ , and  $\mathbf{T}$  are given in Appendix A.

### Adjoint problem

The standard least-squares objective functional is

$$J(\mathbf{u}, \mathbf{s}) = \frac{1}{2} \langle \mathbf{R}\mathbf{u} - \mathbf{d}_{\text{obs}} | \mathbf{R}\mathbf{u} - \mathbf{d}_{\text{obs}} \rangle, \quad (10)$$

where  $\mathbf{u}$  defined in equation 3 is the solution of the forward problem;  $\mathbf{s}$  is the seismic source defined in equation 4;  $\mathbf{R}$  is a sampling operator that restricts the solution to the receiver locations; and  $\mathbf{d}_{\text{obs}}$  is the data recorded at the receivers, which consists of the three velocity components  $v_1$ ,  $v_2$ , and  $v_3$ . Here,  $\langle \cdot | \cdot \rangle$  denotes an inner product.

If we define the augmented functional (Gunzburger, 2003; Oberai et al., 2003; Plessix, 2006) by

$$\begin{aligned}L(\mathbf{u}, \mathbf{u}', \mathbf{q}_1', \mathbf{q}_2', \mathbf{s}) &= J(\mathbf{u}) + \left\langle \mathbf{q}_1' \left| \Lambda \frac{\partial \mathbf{u}'}{\partial t} - \mathbf{A}' \mathbf{u}' - \mathbf{s}' \frac{dw}{dt} \right. \right\rangle \\ &\quad + \langle \mathbf{q}_2' | \mathbf{u}' - \mathbf{T} \mathbf{u} \rangle,\end{aligned}\quad (11)$$

where  $\mathbf{q}_1'$  and  $\mathbf{q}_2'$  are the adjoint wavefields that correspond to the solutions of the constraint equations 5 and 8, respectively, then computing the variation of the augmented functional with respect to the transformed wavefield  $\mathbf{u}'$  gives

$$\begin{aligned}\frac{\partial L}{\partial \mathbf{u}'} &= \int_{\mathbb{R}^3} \mathbf{q}_1'(T) \cdot \Lambda \tilde{\mathbf{u}}'(T) d\mathbf{x} - \left\langle \frac{\partial \mathbf{q}_1'}{\partial t} \right| \Lambda \tilde{\mathbf{u}}' \\ &\quad - \langle \mathbf{q}_1' | \mathbf{A}' \tilde{\mathbf{u}}' \rangle + \langle \mathbf{q}_2' | \tilde{\mathbf{u}}' \rangle,\end{aligned}\quad (12)$$

where  $\tilde{\mathbf{u}}'$  denotes a perturbation of  $\mathbf{u}'$ . To satisfy the first-order necessary conditions for optimization, we set equation 12 to zero, which forces the final condition that  $\mathbf{q}_1'(T) = 0$  and

$$\left\langle -\Lambda \frac{\partial \mathbf{q}_1'}{\partial t} + \mathbf{A}' \mathbf{q}_1' + \mathbf{q}_2' | \tilde{\mathbf{u}}' \right\rangle = 0, \quad (13)$$

because  $\Lambda$  is a diagonal matrix and  $\mathbf{A}'$  is a skew-symmetric operator. Because  $\tilde{\mathbf{u}}'$  is arbitrary, we conclude that

$$\Lambda \frac{\partial \mathbf{q}_1'}{\partial t} - \mathbf{A}' \mathbf{q}_1' = \mathbf{q}_2'. \quad (14)$$

Next, computing the variation of the augmented functional 11 with respect to the solution  $\mathbf{u}$  and applying the first-order necessary condition for optimization implies that

$$\mathbf{q}_2' = (\mathbf{T}^T)^{-1} \mathbf{R}^T (\mathbf{R}\mathbf{u} - \mathbf{d}_{\text{obs}}). \quad (15)$$

Substituting equation 15 into equation 14 to eliminate  $\mathbf{q}_2'$  gives the adjoint equation in the transformed coordinate system

$$\Lambda \frac{\partial \mathbf{q}'_1}{\partial t} - \mathbf{A}' \mathbf{q}'_1 = \mathbf{T}^{T^{-1}} \mathbf{R}^T (\mathbf{R} \mathbf{u} - \mathbf{d}_{\text{obs}}). \quad (16)$$

Because  $\mathbf{q}'_1$  is the transformed adjoint wavefield, we define the adjoint field in the original coordinate system to be

$$\mathbf{q}_1 = \mathbf{T}^{-1} \mathbf{q}'_1 = (r_1, r_2, r_3, \tau_{11}, \tau_{22}, \tau_{33}, \tau_{12}, \tau_{13}, \tau_{23})^T. \quad (17)$$

The first three components  $r_1, r_2$ , and  $r_3$  of  $\mathbf{q}_1$  correspond to the velocity components  $v_1, v_2$ , and  $v_3$  of  $\mathbf{u}$ , whereas the last six components  $\tau_{11}, \tau_{22}, \tau_{33}, \tau_{12}, \tau_{13}$ , and  $\tau_{23}$  of  $\mathbf{q}_1$  correspond to the stresses  $\sigma_{11}, \sigma_{22}, \sigma_{33}, \sigma_{12}, \sigma_{13}$ , and  $\sigma_{23}$ . Thus, in the original coordinate system, the adjoint equation is

$$\frac{\partial \mathbf{q}_1}{\partial t} = \mathbf{A} \mathbf{q}_1 + (\mathbf{T}^T \Lambda \mathbf{T})^{-1} \mathbf{R}^T (\mathbf{R} \mathbf{u} - \mathbf{d}_{\text{obs}}). \quad (18)$$

Note that adjoint equation 18 is identical to the forward problem 2, except that the solution vector  $\mathbf{u}$  has been replaced by the adjoint solution vector  $\mathbf{q}_1$  and the source term of the adjoint problem 18 consists of a transformed residual.

### Gradient computations for the spatial and temporal components of the source

We use the adjoint equation 18 to compute the gradient of the objective functional 10 with respect to the wavelet assuming that the spatial component of the source is a moment tensor that is known. We begin by computing the variation of the augmented functional 11 with respect to the wavelet  $w(t)$ . Because  $\mathbf{q}'_1 = \mathbf{T} \mathbf{q}_1$  and  $\mathbf{s}' = \Lambda \mathbf{T} \mathbf{s}$  in equations 17 and 6, we can write equation 11 as

$$L = J(\mathbf{u}) + \left\langle \mathbf{T} \mathbf{q}_1 \left| \Lambda \frac{\partial \mathbf{u}'}{\partial t} - \mathbf{A}' \mathbf{u}' - \Lambda \mathbf{T} \mathbf{s} \frac{dw}{dt} \right. \right\rangle + \langle \mathbf{T} \mathbf{q}_2 | \mathbf{u}' - \mathbf{T} \mathbf{u} \rangle. \quad (19)$$

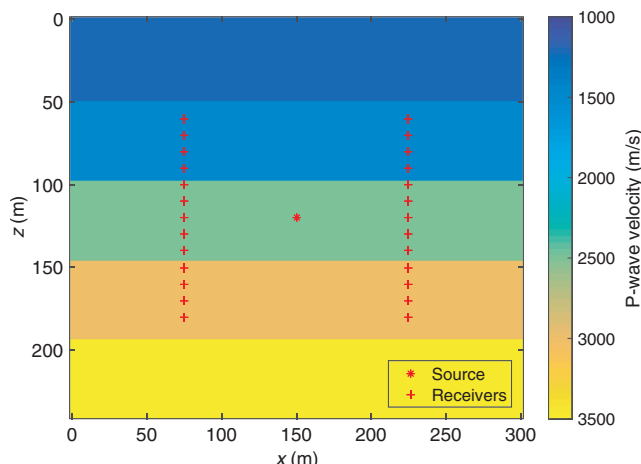


Figure 1. The P-wave velocity for numerical experiments 1 and 2 with the source and receiver positions in the  $xz$ -plane shown.

Performing integration by parts to move the time derivative off of  $w$  gives

$$L = J(\mathbf{u}) + \left\langle \mathbf{T} \mathbf{q}_1 \left| \Lambda \frac{\partial \mathbf{u}'}{\partial t} \right. \right\rangle - \langle \mathbf{T} \mathbf{q}_1 | \mathbf{A}' \mathbf{u}' \rangle + \left\langle \mathbf{T} \frac{\partial \mathbf{q}_1}{\partial t} \left| \Lambda \mathbf{T} \mathbf{s} w \right. \right\rangle + \langle \mathbf{T} \mathbf{q}_2 | \mathbf{u}' - \mathbf{T} \mathbf{u} \rangle. \quad (20)$$

Then, computing the variation of  $L$  with respect to  $w$  gives

$$\frac{\partial L}{\partial w} = \int_{\mathbb{R}^3} \int_0^T \mathbf{T}^T \Lambda \mathbf{T} \frac{\partial \mathbf{q}_1}{\partial t} \cdot \tilde{\mathbf{s} w} dt dx. \quad (21)$$

Replacing  $\tilde{w}$  by a Dirac delta distribution  $\delta$  gives the gradient  $D_w J$  of the objective functional  $J$  with respect to the wavelet  $w$ , namely,

$$D_w J(t) = \int_{\mathbb{R}^3} \mathbf{T}^T \Lambda(\mathbf{x}) \mathbf{T} \frac{\partial \mathbf{q}_1(\mathbf{x}, t)}{\partial t} \cdot \mathbf{s}(\mathbf{x}) d\mathbf{x}. \quad (22)$$

As a special case, suppose that the source is a purely explosive point source located at  $\mathbf{x}_s$ . Then, the moment tensor is given by  $m_{ij} = M \delta(\mathbf{x} - \mathbf{x}_s) \delta_{ij}$ , where  $M$  is the magnitude of the moment tensor,  $\delta(\mathbf{x} - \mathbf{x}_s)$  is a Dirac delta distribution centered at  $\mathbf{x}_s$ , and  $\delta_{ij}$  is the Kronecker delta. The Dirac distribution  $\delta(\mathbf{x} - \mathbf{x}_s)$  encodes the assumption of a point source, whereas the Kronecker delta  $\delta_{ij}$  represents the assumption that the source is explosive; i.e., the moment tensor is the identity matrix. In such a case, the source vector  $\mathbf{s}$  is given by

$$\mathbf{s}(\mathbf{x}) = M(0, 0, 0, \delta(\mathbf{x} - \mathbf{x}_s), \delta(\mathbf{x} - \mathbf{x}_s), \delta(\mathbf{x} - \mathbf{x}_s), 0, 0, 0)^T. \quad (23)$$

Substituting equation 23 into equation 22 and simplifying gives

$$D_w J(t) = \frac{3M}{3\lambda(\mathbf{x}_s) + 2\mu(\mathbf{x}_s)} \left( \frac{\partial q_p(\mathbf{x}_s, t)}{\partial t} \right), \quad (24)$$

where  $q_p = (\tau_{11} + \tau_{22} + \tau_{33})/3$  is the adjoint pressure solution.

We performed the following test to computationally verify the correctness of the gradient calculation. We generated an arbitrary unit vector in the model space. We then computed the directional derivative of the objective functional in the direction given by the unit vector in two different ways: by using the limit definition of the directional derivative and by computing the inner product of the unit vector and the gradient. Both methods yielded the same directional derivative up to machine precision. In addition, the first numerical experiment below demonstrates that the inversion algorithm and the gradient we calculate in this paper recover the wavelet.

Now, we compute the gradient of the objective functional 10 with respect to components of the moment tensor assuming the wavelet  $w(t)$  is a known function of time. We begin by computing the variation of equation 19 with respect to a given component  $m_{ij}$  of the moment tensor. When computing the variation with respect to  $m_{ij}$ , every term of equation 19 will vanish except for the term containing  $s$ . Thus, we only need to consider the term

$$-\left\langle \mathbf{T}\mathbf{q}_1 \left| \Lambda \mathbf{T}\mathbf{s} \frac{dw}{dt} \right. \right\rangle. \quad (25)$$

Applying the adjoint operators  $\Lambda^T = \Lambda$  and  $\mathbf{T}^T$ , we obtain

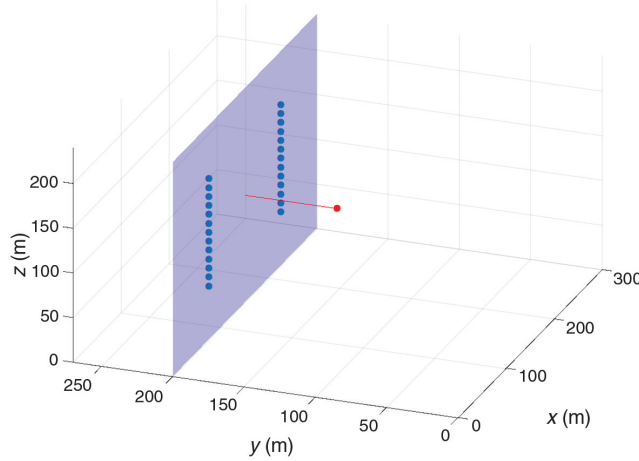


Figure 2. Locations of the source (red) and receivers (blue) in three dimensions for experiments 1–3.

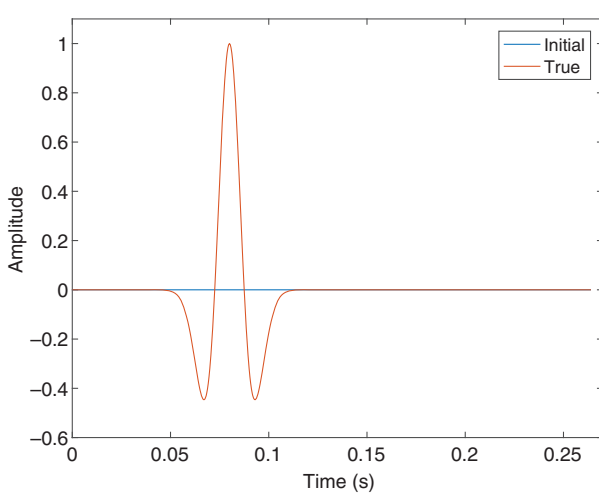


Figure 3. True and initial wavelet for numerical experiments 1–3.

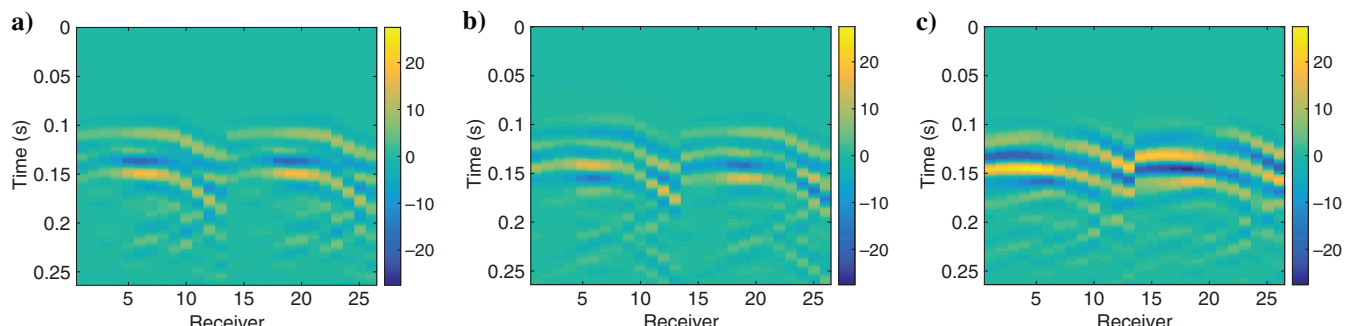


Figure 4. Recorded velocity data for numerical experiment 1: (a)  $v_1$  component, (b)  $v_2$  component, and (c)  $v_3$  component.

$$\begin{aligned} -\left\langle \mathbf{T}^T \Lambda \mathbf{T}\mathbf{q}_1 \left| \mathbf{s} \frac{dw}{dt} \right. \right\rangle &= -\int_0^T \int_{\mathbb{R}^3} \mathbf{T}^T \Lambda \mathbf{T}\mathbf{q}_1(\mathbf{x}, t) \cdot \mathbf{s}(\mathbf{x}) \frac{dw}{dt} d\mathbf{x} dt \\ &= -\int_0^T \frac{dw}{dt} \int_{\mathbb{R}^3} \frac{1}{\mu(3\lambda+2\mu)} \\ &\times \left( (\lambda+\mu)\tau_{11} - \frac{1}{2}\lambda\tau_{22} - \frac{1}{2}\lambda\tau_{33} \right) m_{11} \\ &+ \frac{1}{\mu(3\lambda+2\mu)} \left( -\frac{1}{2}\lambda\tau_{11} + (\lambda+\mu)\tau_{22} - \frac{1}{2}\lambda\tau_{33} \right) m_{22} \\ &+ \frac{1}{\mu(3\lambda+2\mu)} \left( -\frac{1}{2}\lambda\tau_{11} - \frac{1}{2}\lambda\tau_{22} + (\lambda+\mu)\tau_{33} \right) m_{33} \\ &+ \frac{1}{\mu} \tau_{12} m_{12} + \frac{1}{\mu} \tau_{13} m_{13} + \frac{1}{\mu} \tau_{23} m_{23} dx dt. \end{aligned} \quad (26)$$

Computing the variation of equation 26 with respect to each component of the moment tensor yields the following gradients:

$$\begin{aligned} \frac{\partial J}{\partial m_{11}}(\mathbf{x}) &= -\frac{1}{\mu(3\lambda+2\mu)} \int_0^T \left( (\lambda+\mu)\tau_{11}(\mathbf{x}, t) \right. \\ &\quad \left. - \frac{\lambda}{2}\tau_{22}(\mathbf{x}, t) - \frac{\lambda}{2}\tau_{33}(\mathbf{x}, t) \right) \frac{dw(t)}{dt} dt, \end{aligned} \quad (27)$$

$$\begin{aligned} \frac{\partial J}{\partial m_{22}}(\mathbf{x}) &= -\frac{1}{\mu(3\lambda+2\mu)} \int_0^T \left( -\frac{\lambda}{2}\tau_{11}(\mathbf{x}, t) \right. \\ &\quad \left. + (\lambda+\mu)\tau_{22}(\mathbf{x}, t) - \frac{\lambda}{2}\tau_{33}(\mathbf{x}, t) \right) \frac{dw(t)}{dt} dt, \end{aligned} \quad (28)$$

$$\begin{aligned} \frac{\partial J}{\partial m_{33}}(\mathbf{x}) &= -\frac{1}{\mu(3\lambda+2\mu)} \int_0^T \left( -\frac{\lambda}{2}\tau_{11}(\mathbf{x}, t) - \frac{\lambda}{2}\tau_{22}(\mathbf{x}, t) \right. \\ &\quad \left. + (\lambda+\mu)\tau_{33}(\mathbf{x}, t) \right) \frac{dw(t)}{dt} dt, \end{aligned} \quad (29)$$

$$\frac{\partial J}{\partial m_{12}}(\mathbf{x}) = -\int_0^T \frac{1}{\mu} \tau_{12}(\mathbf{x}, t) \frac{dw(t)}{dt} dt, \quad (30)$$

$$\frac{\partial J}{\partial m_{13}}(\mathbf{x}) = - \int_0^T \frac{1}{\mu} \tau_{13}(\mathbf{x}, t) \frac{dw(t)}{dt} dt, \quad (31)$$

$$\frac{\partial J}{\partial m_{23}}(\mathbf{x}) = - \int_0^T \frac{1}{\mu} \tau_{23}(\mathbf{x}, t) \frac{dw(t)}{dt} dt, \quad (32)$$

where the positional dependencies have been omitted from  $\lambda(\mathbf{x})$  and  $\mu(\mathbf{x})$ . The gradient computation for a directed force source is given in Appendix A.

## NUMERICAL RESULTS

In this section, we describe several inversion experiments that rely on the theory presented in the previous section for calculation of the gradient. The kernel of the inversion, a wave equation solver originally developed at Sandia National Laboratories (Sleefe et al., 1998; Minkoff, 2002), uses a second order in time and fourth order in space staggered finite-difference scheme for solution of the velocity-stress formulation of the wave equation. We substantially

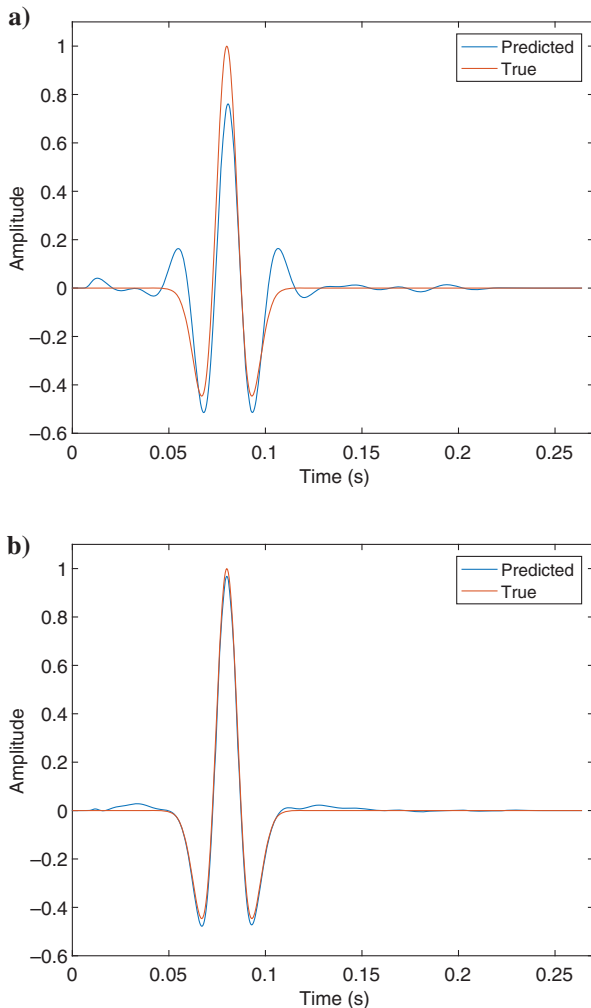


Figure 5. Inversion results for numerical experiment 1: (a) iteration 1 and (b) iteration 5.

modified the code, which was originally developed to solve the forward problem only, to perform FWI using the gradients computed in the previous section. The experiments we describe in this section involve inverting for either the complete temporal component (including the time evolution and amplitude of the source) or the entire spatial description (the distribution of source events in space and the moment tensor components at each point in the domain). The temporal component is a function of a single variable: time. The spatial component, however, is a function of three variables, and so we display the spatial component as slices of a 3D cube. The optimization was performed via the conjugate gradient method. We begin by demonstrating the accuracy of the technique in a simple case, and we gradually move to more realistic microseismic source inversion experiments.

### Inverting for a Ricker wavelet in time assuming the spatial component of the source is a known moment tensor

In the first numerical experiment, we assume that the spatial description of the source and the elastic parameters of the medium (P- and S-wave velocities and density) are known, and we invert for the wavelet only. The domain is a 3D layered medium defined on a cube with dimensions  $[0 \text{ m}, 300 \text{ m}] \times [0 \text{ m}, 270 \text{ m}] \times [0 \text{ m}, 240 \text{ m}]$ , and the computational mesh is discretized into  $101 \times 91 \times 81$  grid-points (grid spacing of 3 m). We used absorbing boundary conditions to avoid boundary reflections off the edges of the computational domain. The layered medium is described by a P-wave velocity, which varies from 1200 to 3500 m/s in depth, as shown in Figure 1. Similarly, the S-wave velocity varies from 600 to 2250 m/s. The density is assumed constant at  $2000 \text{ kg/m}^3$  for these numerical experiments, although nothing about the theory requires a constant density medium. A point source located at the center of the domain,  $(x, y, z) = (150 \text{ m}, 135 \text{ m}, 120 \text{ m})$ , is characterized by the pure strike-slip moment tensor

$$\begin{bmatrix} 0 & 1 & 0 \\ 1 & 0 & 0 \\ 0 & 0 & 0 \end{bmatrix}. \quad (33)$$

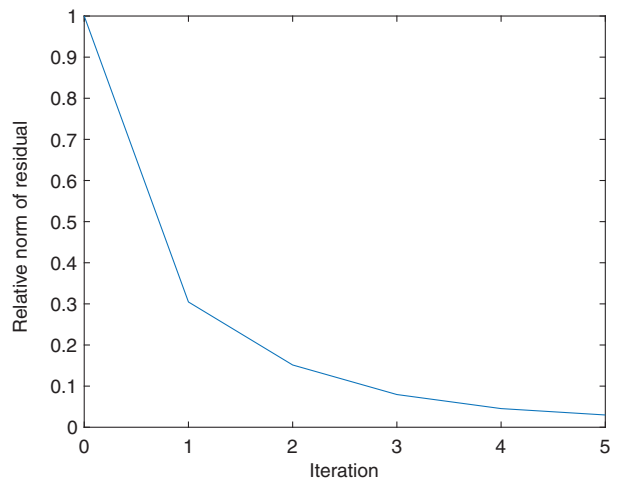


Figure 6. Relative norm of the residual versus iteration number for numerical experiment 1.

In other words, the source term  $\mathbf{s}(\mathbf{x})$  defined in equation 4 is given by

$$\mathbf{s}(\mathbf{x}) = \begin{cases} (0, 0, 0, 0, 0, 0, 1, 0, 0)^T & \text{if } \mathbf{x} = (150, 135, 120) \\ (0, 0, 0, 0, 0, 0, 0, 0, 0)^T & \text{otherwise} \end{cases}. \quad (34)$$

Dual-borehole receiver arrays, shown in Figure 2, are located at  $(x, y) = (75 \text{ m}, 200 \text{ m})$  and  $(x, y) = (225 \text{ m}, 200 \text{ m})$  with each array containing 13 receivers spaced 10 m apart in the  $z$ -direction from  $z = 60$  to  $z = 180 \text{ m}$ . The true wavelet is a 30 Hz Ricker wavelet (Figure 3, red curve), and the initial estimate of the wavelet is taken to be identically zero (Figure 3, blue curve). The total simulation time

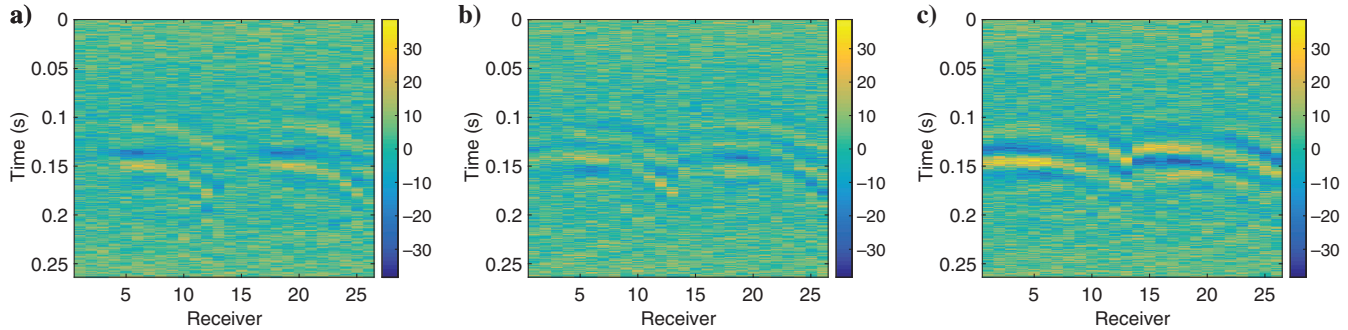


Figure 7. Recorded velocity data with added noise for numerical experiment 2: (a)  $v_1$  component, (b)  $v_2$  component, and (c)  $v_3$  component.

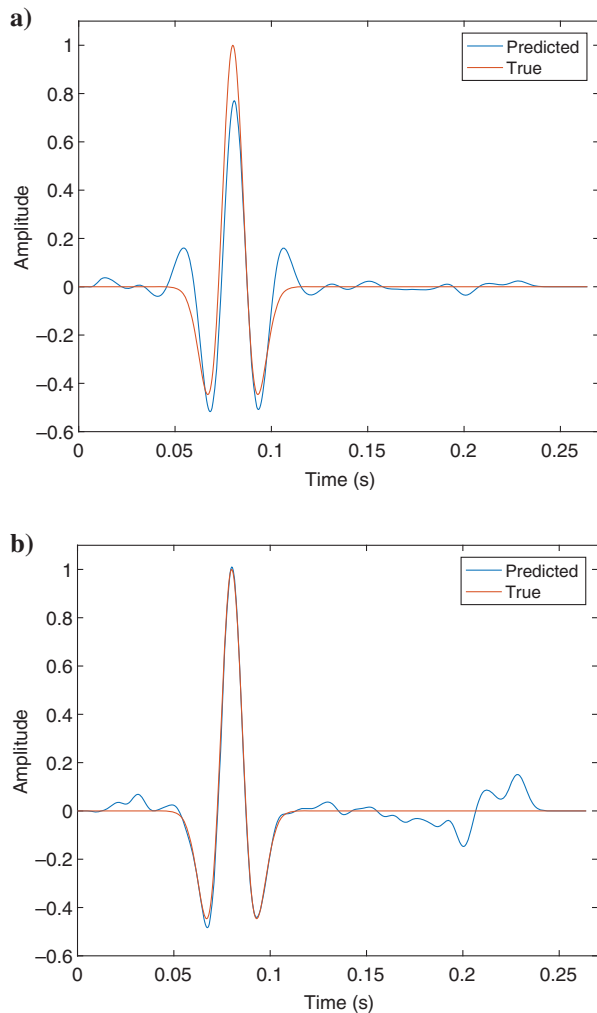


Figure 8. Inversion results for numerical experiment 2 using noisy data: (a) iteration 1 and (b) iteration 5.

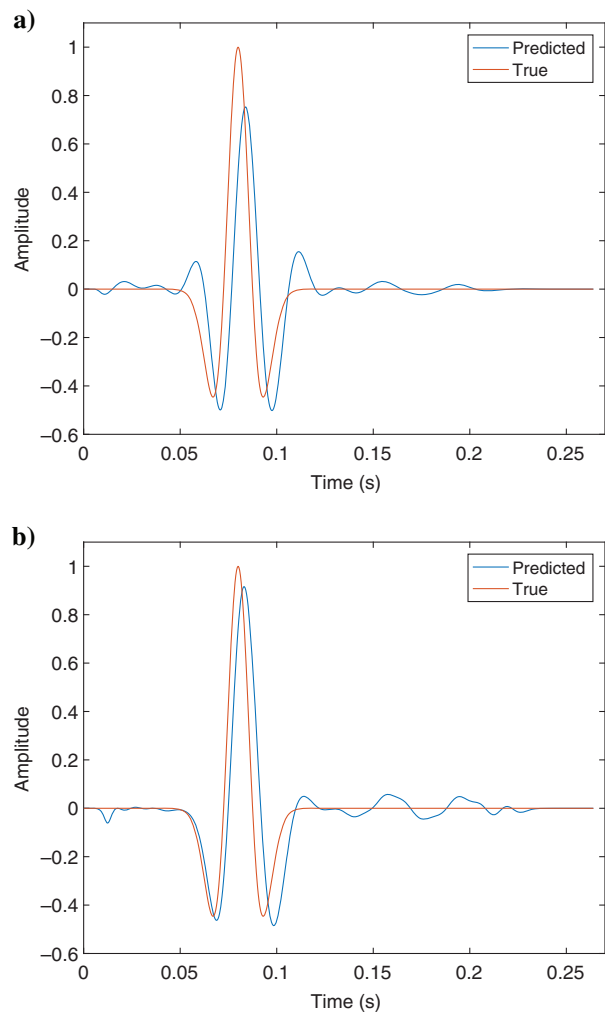


Figure 9. Inversion results for numerical experiment 3: (a) iteration 1 and (b) iteration 15.

is [0 s, 0.264 s] with a step size of 0.0004 s. The recorded data are shown in Figure 4.

The temporal component of the source term in equation 2 contains a time derivative of the wavelet, and this differentiation introduces some roughness in the resulting modeled wavefields. Therefore, we apply a Gaussian filter to smooth the numerically differentiated waveform and a Planck-taper window to ensure causality of the wavelet. Despite the very poor initial guess, we see a

**Table 1. Earth model parameters for layered medium experiment 3.**

Depth (m)	P-wave velocity (m/s)		S-wave velocity (m/s)	
	True	Perturbed	True	Perturbed
0–48	1200	1000	600	500
48–96	1500	1650	1000	1100
96–144	2500	2600	1500	1650
144–192	3000	2900	2000	1800
192–240	3500	3300	2250	2100

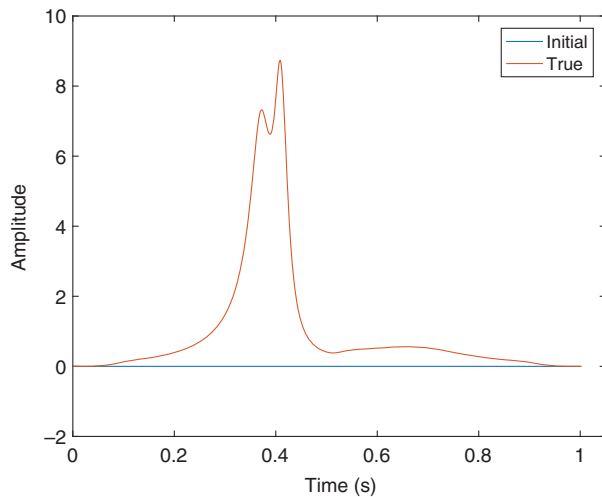


Figure 10. True (CFRAC) and initial wavelet for numerical experiments 4–6.

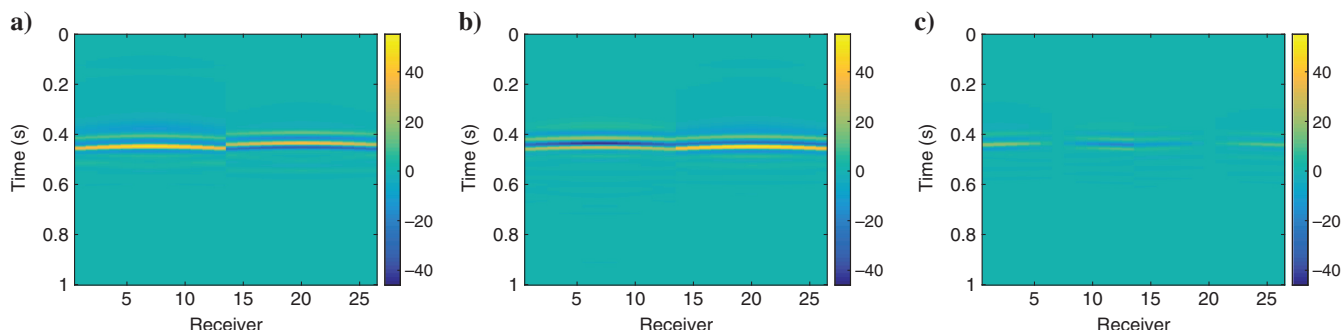


Figure 11. Recorded velocity data for numerical experiment 4: (a)  $v_1$  component, (b)  $v_2$  component, and (c)  $v_3$  component.

striking match after only one inversion iteration, and the algorithm recovers the true wavelet by the fifth iteration (see Figure 5). A plot of the norm of the residual versus the iteration number is shown in Figure 6.

In numerical experiment 2, we repeat the previous experiment to investigate how well the algorithm handles noisy data. Uniform noise was added to the data, and the result was filtered to remove frequencies less than 4 Hz. The data, which are shown in Figure 7, have a 0.41 signal-to-noise ratio (defined as the maximum amplitude of the signal divided by the variance of the noise). The inversion results at iterations 1 and 5 are shown in Figure 8. The predicted wavelet is largely recovered by the algorithm.

In numerical experiment 3, we investigate the effect of assuming a fixed but incorrect velocity model on the estimated wavelet. The recorded data are generated with the true velocity model, whereas the inversion algorithm uses the perturbed velocity model (see Table 1). The density is again assumed to be known and constant. All other experimental parameters are the same as in experiments 1 and 2. The results of the inversion are shown in Figure 9. Due to the inaccuracy in the velocity model, the estimated source is shifted in time. However, the results are still surprisingly accurate after only a few iterations.

#### Inverting for a more complex wavelet in time assuming the spatial component of the source is a known moment tensor

In the next three numerical experiments, we invert for the moment tensor and wavelet of a realistic microseismic source generated using the Complex Fracture ReseArch Code (CFRAC) (McClure and Horne, 2011). CFRAC models coupled flow and deformation, specifically hydraulic injection of a single-phase fluid into an impermeable, isotropic medium with discrete fractures. The deformation is modeled in a 2D plane assuming quasistatic equilibrium. For these three inversion experiments, the medium is assumed homogeneous. The P-wave velocity  $V_p = 4375 \text{ m/s}$ , S-wave velocity  $V_s = 2500 \text{ m/s}$ , and density  $\rho = 2500 \text{ kg/m}^3$ . The far-field stress state is defined by the two normal stresses  $\sigma_{11} = 65 \text{ MPa}$  and  $\sigma_{22} = 100 \text{ MPa}$  and the shear stress of  $\sigma_{12} = 0 \text{ MPa}$ . The in situ pressure within the fracture prior to injection is 40 MPa. For this flow and deformation experiment, the fracture is oriented at  $60^\circ$  relative to  $\sigma_{11}$  and fluid (water) is injected into the fracture via an open, horizontal wellbore at a maximum pressure of 70 MPa and a maximum rate of 80 kg/s for 1800 s. The model exhibits episodes of increasing and decreasing injection rate coupled with periods of movement along the fracture indicative

of stick-slip behavior. Microseismic events are defined to have initiated when the sliding velocity exceeds 0.005 m/s and to have arrested when the velocity drops less than 0.0025 m/s (McClure and Horne, 2011; McChesney et al., 2016). The single microseismic event we use as the source in these three inversion experiments is just one of many microseismic events to result from the CFRAC simulation. For numerical experiments 4–6, the microseism is a point source with the radiation pattern defined by the simulated failure of the fracture. The temporal component of the source, which we refer to in this work as the CFRAC wavelet, is shown in Figure 10 (red curve).

In numerical experiment 4, we assume that the microseismic source is located at the center of the domain,  $(x, y, z) = (150 \text{ m}, 135 \text{ m}, 120 \text{ m})$ . The radiation pattern is characterized by the moment tensor

$$\begin{bmatrix} \frac{\sqrt{3}}{2} & -\frac{1}{2} & 0 \\ -\frac{1}{2} & -\frac{\sqrt{3}}{2} & 0 \\ 0 & 0 & 0 \end{bmatrix}, \quad (35)$$

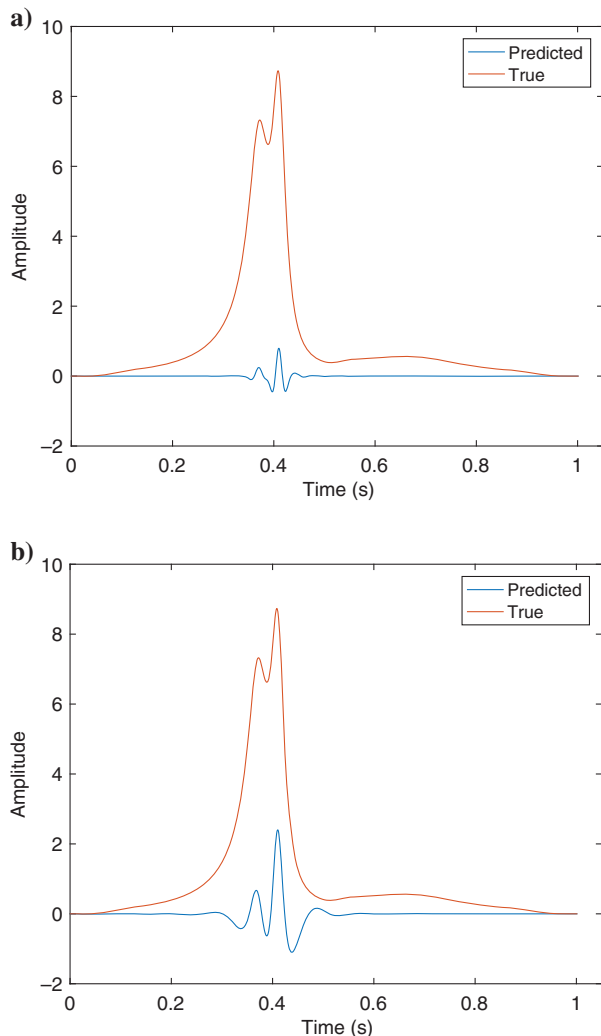


Figure 12. Inversion results for numerical experiment 4: (a) iteration 1 and (b) iteration 50.

which represents a pure strike-slip fault with the source term  $\mathbf{s}(\mathbf{x})$  given by

$$\mathbf{s}(\mathbf{x}) = \begin{cases} \left(0, 0, 0, \frac{\sqrt{3}}{2}, -\frac{\sqrt{3}}{2}, 0, -\frac{1}{2}, 0, 0\right)^T & \text{if } \mathbf{x} = (150, 135, 120) \\ (0, 0, 0, 0, 0, 0, 0, 0, 0)^T & \text{otherwise} \end{cases}. \quad (36)$$

The total simulation time is [0 s, 1.0021 s] with a time step of 0.0001 s. The domain, mesh size, and receiver locations are identical to those used in numerical experiments 1–3. The recorded data are shown in Figure 11.

The result of the inversion is shown in Figure 12, and a plot of the norm of the residual versus the iteration number is shown in Figure 13. The algorithm correctly determines the peak time of the wavelet, but the shape and amplitude of the predicted wavelet are not as accurate as in the previous examples. The low-frequency content and the shape of the CFRAC wavelet make the inversion more difficult. The frequency content of the CFRAC wavelet is shown in Figure 14a (the red curve), and the source clearly has a sizable 0 Hz component. In comparing the predicted wavelet with the true source wavelet (Figure 12), we observe that the shape of the predicted wavelet partially matches the true wavelet, but that significant low-frequency content is missing. The low-frequency information required to completely describe the true wavelet is not present in the observed data (see Figure 14a, the blue curve). If we filter the bandwidth of the true wavelet to the range of frequencies with appreciable amplitude in the observed data, we see that the predicted wavelet matches this filtered version of the true wavelet very well (see Figure 14b). Thus, our algorithm successfully recovers as much of the true wavelet as possible given the energy in the observed data.

#### Inverting for the spatial component of the source assuming the wavelet is known

In numerical experiment 5, we invert for the moment tensor (as given in equation 35) assuming that the wavelet is known to be the CFRAC wavelet from numerical experiment 4. The domain for this numerical experiment is [0 m, 240 m]  $\times$  [0 m, 180 m]  $\times$  [0 m, 120 m].

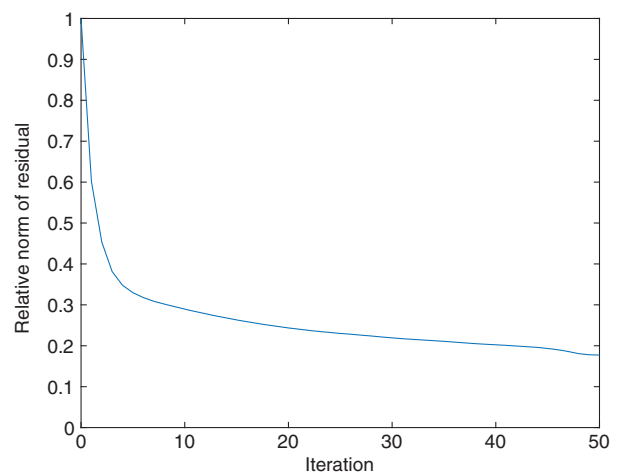


Figure 13. Relative norm of residual versus iteration number for numerical experiment 4.

Two vertical receiver arrays are located at  $(x, y) = (60 \text{ m}, 135 \text{ m})$  and  $(x, y) = (180 \text{ m}, 135 \text{ m})$  with each array containing seven receivers spaced 10 m apart in the  $z$ -direction from  $z = 30$  to  $z = 90$  m. The mesh is  $81 \times 61 \times 41$  gridpoints, which retains the 3 m spacing between nodes as in the previous numerical experiments. The medium parameters and wavelet are identical to those in numerical experiment 4, and the recorded data are generated via a point source at the center of the domain with the same moment tensor as in experiment 4. We invert for the six independent components of the moment tensor source parameterization  $m_{11}, m_{22}, m_{33}, m_{12}, m_{13}$ , and  $m_{23}$ , where each  $m_{ij}$  is a function of position. After discretization, each  $m_{ij}$  is a 3D volume defining the stress perturbation associated with the source at each point in the domain. The wavefields generated by these 3D source cubes can be thought of as coming from a linear combination of point sources located at every gridpoint in the domain. The elements of the moment tensors are defined by the amplitudes of the cubes at that gridpoint. In Figure 15, we show slices of the  $m_{11}$  moment tensor cube along the three planes:  $z = 15$ ,  $z = 60$ , and  $z = 105$  m after 20 iterations of the inversion algorithm. Because the source location for the recorded data is  $(x, y, z) = (120 \text{ m}, 90 \text{ m}, 60 \text{ m})$ , we expect the results to be focused in the center of the slice at  $z = 60$  m, which is indeed the case. The center slice of Figure 15 shows a concentration of positive energy at the source location, reflecting the fact that for the true source,  $m_{11}(120, 90, 60) = \sqrt{3}/2$ . We note that we have not implemented any regularization in this work. Adding a sparsity constraint similar to what is done in Gao et al. (2017) would likely focus the source better. A plot of the norm of the residual versus iteration number is shown in Figure 16.

In numerical experiment 6, we consider the case in which there are four vertical receiver arrays rather than two. The four receiver

Figure 14. CFRAC wavelets and recorded data from numerical experiment 4. (a) The frequency domain comparison of the CFRAC wavelet (red), the recorded data (blue), and the filtered CFRAC wavelet (black dashed). (b) The time domain comparison of the CFRAC wavelet (red), the predicted wavelet (blue), and the filtered CFRAC wavelet (black dashed).

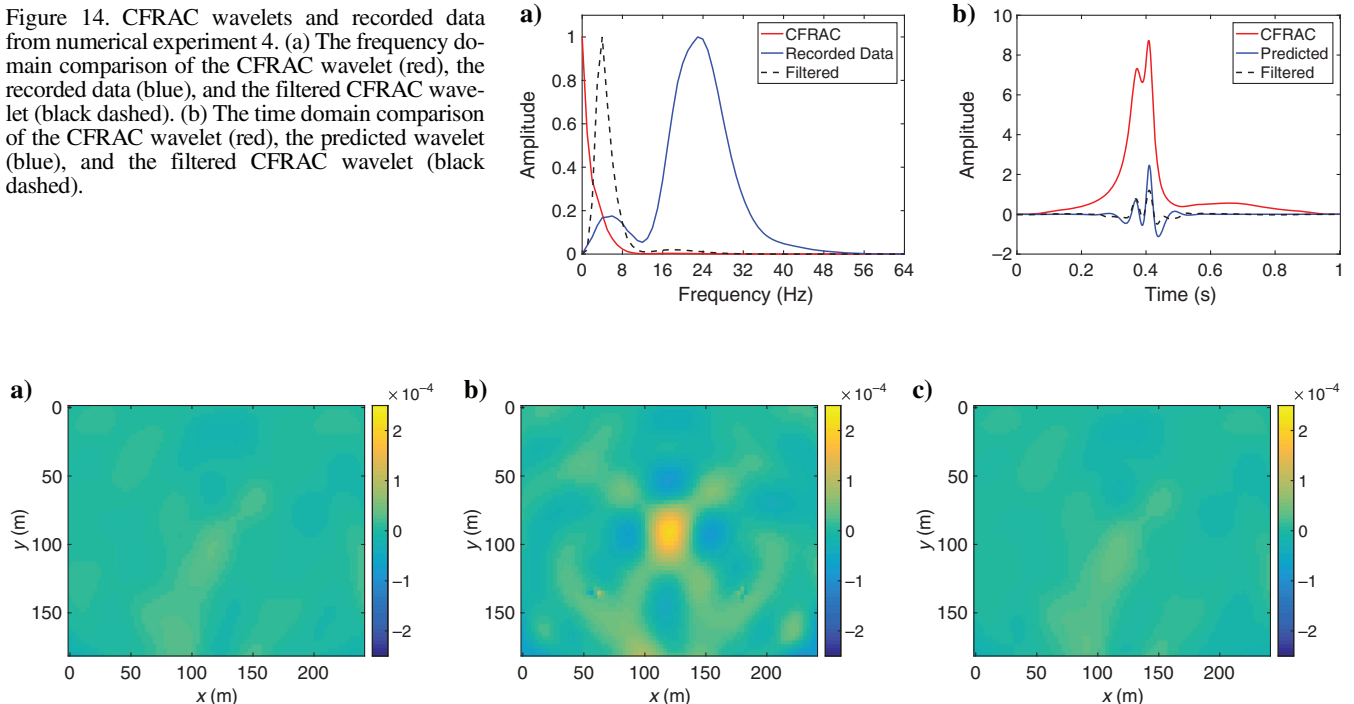


Figure 15. Predicted  $m_{11}$  spatial component of the source at inversion iteration 20 for three different depth slices using two receiver arrays: (a)  $z = 15$  m, (b)  $z = 60$  m, and (c)  $z = 105$  m.

arrays are located at  $(x, y) = (60 \text{ m}, 45 \text{ m})$ ,  $(x, y) = (180 \text{ m}, 45 \text{ m})$ ,  $(x, y) = (60 \text{ m}, 135 \text{ m})$ , and  $(x, y) = (180 \text{ m}, 135 \text{ m})$  with each array containing seven receivers spaced 10 m apart in the  $z$ -direction from  $z = 30$  to  $z = 90$  m. The predicted  $m_{11}, m_{22}, m_{12}$ , and  $m_{33}$  components are shown in Figures 17, 18, 19, and 20, respectively. The result is more symmetrical than the result obtained in the case of two vertical receiver arrays. The center slice of Figure 17 again shows a concentration of positive energy at the source location, whereas the center of Figure 18 shows a concentration of negative energy at the same location, which corresponds to the true value of  $m_{22}(120, 90, 60) = -\sqrt{3}/2$ . Figure 19 shows that the predicted  $m_{12}$

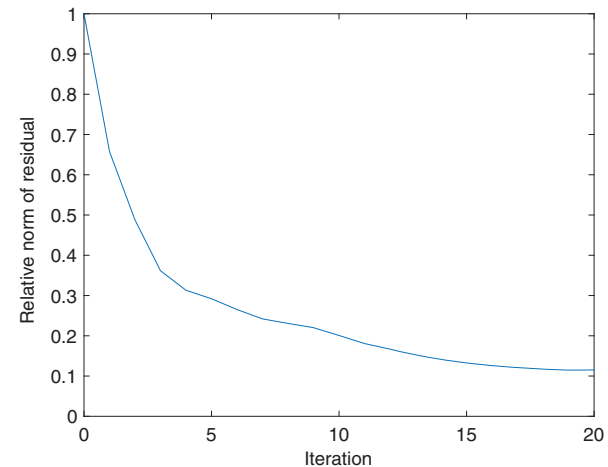


Figure 16. Relative norm of residual versus iteration number for numerical experiment 5.

component focuses at the correct plane. Finally, recall that  $m_{33}$ ,  $m_{13}$ , and  $m_{23}$  are all identically zero. The inversion predicts these components well as is illustrated in Figure 20, which shows an absence of energy for the estimated  $m_{33}$  component; results for  $m_{13}$  and  $m_{23}$ , which are not shown, are similar. Figure 21a shows the amplitude of  $m_{11}$ ,  $m_{22}$ , and  $m_{12}$  along the line  $(x, 90, 60)$ . The  $m_{11}$  component should reach a maximum amplitude of  $\sqrt{3}/2$  at  $x = 120$  m, the  $m_{22}$  component should reach a minimum value of  $-\sqrt{3}/2$  at  $x = 120$  m, and the  $m_{12}$  component should reach a minimum value of  $-1/2$  at  $x = 120$  m. Although the amplitudes are off by a scaling factor, the  $m_{11}$  and  $m_{22}$  components have almost equal amplitudes and opposite signs as expected. Also as expected, the  $m_{12}$  component has the correct sign and is smaller in amplitude than  $m_{11}$  or

$m_{22}$ . Figure 21b shows the amplitude of the same components along the line  $(120, y, 60)$ . Each component should attain its maximum or minimum value at  $y = 90$  m.

In numerical experiment 7, we use a distributed spatial source in the shape of an ellipse. We define the geometry of this ellipse to model a fracture with strike, dip, and rake consistent with the true moment tensor from numerical experiment 1, namely,

$$\begin{bmatrix} 0 & 1 & 0 \\ 1 & 0 & 0 \\ 0 & 0 & 0 \end{bmatrix}. \quad (37)$$

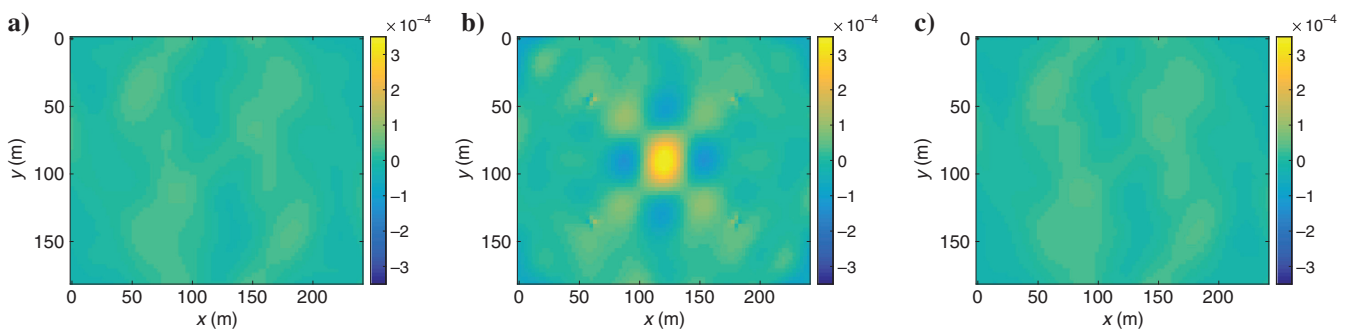


Figure 17. Predicted  $m_{11}$  spatial component of the source at iteration 20 for three different depth slices using four receiver arrays: (a)  $z = 15$  m, (b)  $z = 60$  m, and (c)  $z = 105$  m.

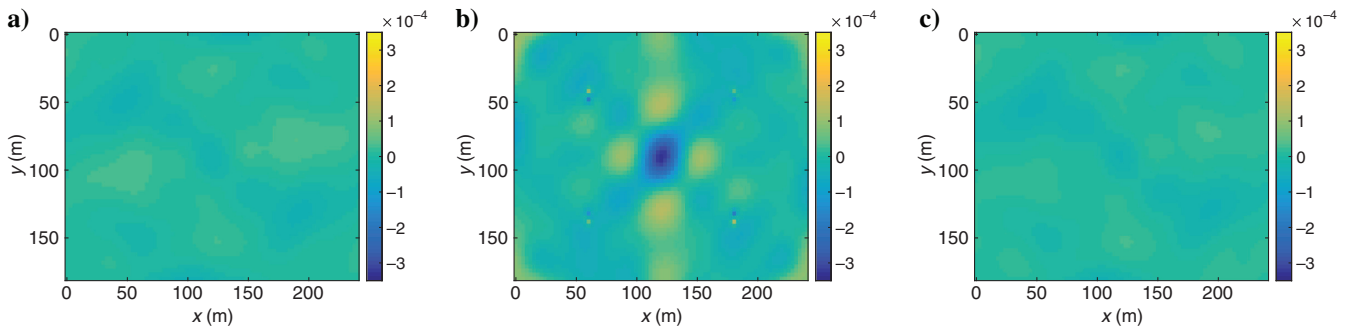


Figure 18. Predicted  $m_{22}$  spatial component of the source at iteration 20 for three different depth slices using four receiver arrays: (a)  $z = 15$  m, (b)  $z = 60$  m, and (c)  $z = 105$  m.

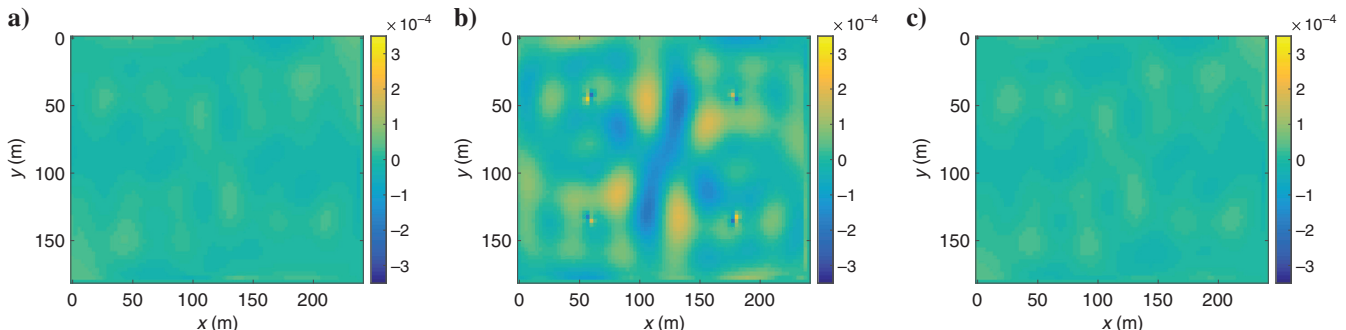


Figure 19. Predicted  $m_{12}$  spatial component of the source at iteration 20 for three different depth slices using four receiver arrays: (a)  $z = 15$  m, (b)  $z = 60$  m, and (c)  $z = 105$  m.

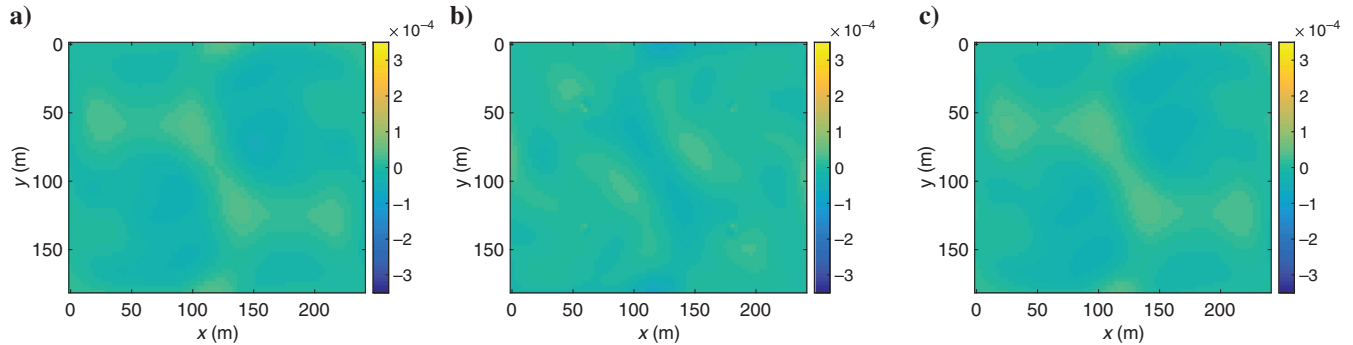


Figure 20. Predicted  $m_{33}$  spatial component of the source at iteration 20 for three different depth slices using four receiver arrays: (a)  $z = 15$  m, (b)  $z = 60$  m, and (c)  $z = 105$  m.

Figure 21. One-dimensional slices of the predicted components of the moment tensor for numerical experiment 6 along (a) the line  $(x, 90, 60)$  and (b) the line  $(120, y, 60)$ .

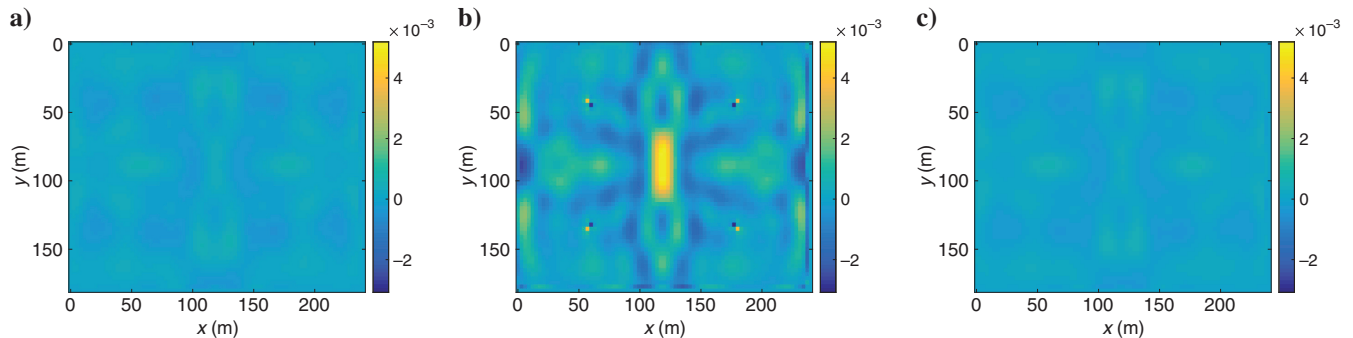
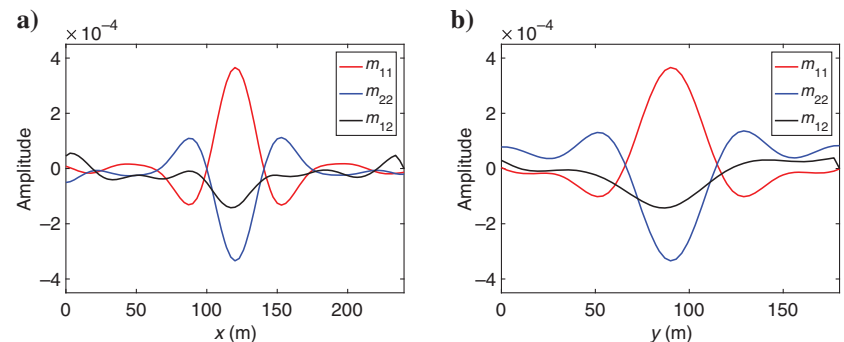


Figure 22. The  $xy$  slices of the predicted  $m_{12}$  spatial component of the distributed source in numerical experiment 7: (a)  $z = 15$  m, (b)  $z = 60$  m, and (c)  $z = 105$  m.

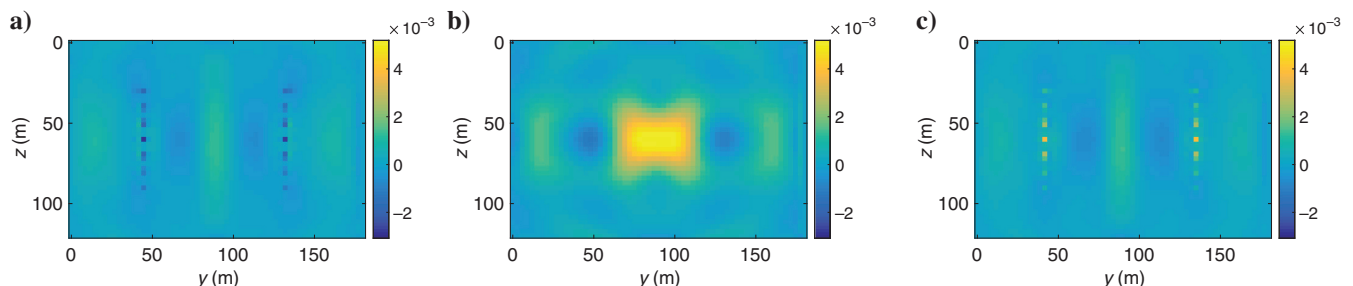


Figure 23. The  $yz$  slices of the predicted  $m_{12}$  spatial component of the distributed source in numerical experiment 7: (a)  $x = 60$  m, (b)  $x = 120$  m, and (c)  $x = 180$  m.

The fracture is centered at (120 m, 90 m, 60 m) and extends from 66 to 114 m in the  $y$ -direction and from 54 to 66 m in the  $z$ -direction. We use four vertical receiver arrays as in numerical experiment 6, and the temporal component of the source is the 30 Hz Ricker wavelet used in numerical experiments 1–3. The sense of motion at every point on the fracture is defined by the moment tensor given above. The distribution of focused energy in the predicted elements of the moment tensor provides information on the geometry of the fracture. The magnitude and sign of the elements describe the sense of motion at each element along the fracture. Figure 22 shows slices parallel to the  $xy$ -plane of the predicted  $m_{12}$  component of the moment tensor. Figure 23 shows slices parallel to the  $yz$ -plane. This result illustrates the capability of this inversion scheme to not only recover the focal mechanism of failure events but also the geometry of the failure plane.

Because our inversion is attempting to recover a complete source description, the resulting solution will include information about not just the moment tensor and wavelet but also the earth response, receiver coupling, and focal sphere sampling of the observed data. Any bias in the initial guess for the moment tensor or wavelet would result in compensation by the other parameter.

## CONCLUSION

We use FWI and a self-adjoint form of the elastic-wave equations to estimate the temporal and spatial components of a microseismic source assuming the other is known. For this separable source, we derive the gradient of the objective functional with respect to the complete source-time function, a distributed source in space with a moment tensor estimate at every point in the domain, or a directed force source. We demonstrate the accuracy of our approach by inverting for a Ricker wavelet with and without noise as well as in the presence of a velocity error. We also investigate the challenges of applying this inversion technique to realistic microseismic events generated from coupled flow and deformation modeling. Despite the combination of a zero initial guess and the particularly challenging nature of the low-frequency wavelet, the time-domain inversion produces a robust solution given the limited frequency content in the data. We also demonstrate the ability of the inversion algorithm to determine a complete description of the source distributed in space. Specifically, an elliptical source modeling a rupture patch along a fault is well-recovered in our algorithm. Future work would include simultaneous inversion for the source-time function and the distributed moment tensor source in space, which would require regularization to ensure that the trade-off in space and time does not cause poorly focused estimates.

## ACKNOWLEDGMENTS

We thank D. Aldridge of Sandia National Laboratories for allowing us to use the wave equation solver he developed and for extremely useful discussions about the code. We also thank M. McClure for providing us with the CFRAC code to model the microseismic event used in experiments 4–6. Finally, we thank several anonymous referees whose thorough reviewing substantially improved this paper.

## APPENDIX A

### OPERATORS INVOLVED IN THE CHANGE OF VARIABLES

The differential operator  $\mathbf{A}$  is

$$\mathbf{A} = \begin{bmatrix} 0 & 0 & 0 & \frac{1}{\rho}\partial_1 & 0 & 0 & \frac{1}{\rho}\partial_2 & \frac{1}{\rho}\partial_3 & 0 \\ 0 & 0 & 0 & 0 & \frac{1}{\rho}\partial_2 & 0 & \frac{1}{\rho}\partial_1 & 0 & \frac{1}{\rho}\partial_3 \\ 0 & 0 & 0 & 0 & 0 & \frac{1}{\rho}\partial_3 & 0 & \frac{1}{\rho}\partial_1 & \frac{1}{\rho}\partial_2 \\ (\lambda+2\mu)\partial_1 & \lambda\partial_2 & \lambda\partial_3 & 0 & 0 & 0 & 0 & 0 & 0 \\ \lambda\partial_1 & (\lambda+2\mu)\partial_2 & \lambda\partial_3 & 0 & 0 & 0 & 0 & 0 & 0 \\ \lambda\partial_1 & \lambda\partial_2 & (\lambda+2\mu)\partial_3 & 0 & 0 & 0 & 0 & 0 & 0 \\ \mu\partial_2 & \mu\partial_1 & 0 & 0 & 0 & 0 & 0 & 0 & 0 \\ \mu\partial_3 & 0 & \mu\partial_1 & 0 & 0 & 0 & 0 & 0 & 0 \\ 0 & \mu\partial_3 & \mu\partial_2 & 0 & 0 & 0 & 0 & 0 & 0 \end{bmatrix}. \quad (\text{A-1})$$

The linear transformation  $\mathbf{T}$  is

$$\mathbf{T} = \begin{bmatrix} 1 & 0 & 0 & 0 & 0 & 0 & 0 & 0 & 0 \\ 0 & 1 & 0 & 0 & 0 & 0 & 0 & 0 & 0 \\ 0 & 0 & 1 & 0 & 0 & 0 & 0 & 0 & 0 \\ 0 & 0 & 0 & \frac{1}{\sqrt{3}} & \frac{1}{\sqrt{3}} & \frac{1}{\sqrt{3}} & 0 & 0 & 0 \\ 0 & 0 & 0 & -\frac{1}{\sqrt{6}} & -\frac{1}{\sqrt{6}} & \frac{2}{\sqrt{6}} & 0 & 0 & 0 \\ 0 & 0 & 0 & -\frac{1}{\sqrt{2}} & \frac{1}{\sqrt{2}} & 0 & 0 & 0 & 0 \\ 0 & 0 & 0 & 0 & 0 & 0 & \sqrt{2} & 0 & 0 \\ 0 & 0 & 0 & 0 & 0 & 0 & 0 & \sqrt{2} & 0 \\ 0 & 0 & 0 & 0 & 0 & 0 & 0 & 0 & \sqrt{2} \end{bmatrix}. \quad (\text{A-2})$$

The transformed differential operator  $\mathbf{A}'$  is

$$\mathbf{A}' = \Delta \mathbf{T} \mathbf{A} \mathbf{T}^{-1}$$

$$= \begin{bmatrix} 0 & 0 & 0 & \frac{\partial_1}{\sqrt{3}} & -\frac{\partial_1}{\sqrt{6}} & -\frac{\partial_1}{\sqrt{2}} & \frac{\partial_2}{\sqrt{2}} & \frac{\partial_3}{\sqrt{2}} & 0 \\ 0 & 0 & 0 & \frac{\partial_2}{\sqrt{3}} & -\frac{\partial_2}{\sqrt{6}} & \frac{\partial_2}{\sqrt{2}} & \frac{\partial_3}{\sqrt{2}} & 0 & \frac{\partial_3}{\sqrt{2}} \\ 0 & 0 & 0 & \frac{\partial_3}{\sqrt{3}} & \frac{2\partial_3}{\sqrt{6}} & 0 & 0 & \frac{\partial_1}{\sqrt{2}} & \frac{\partial_2}{\sqrt{2}} \\ \frac{\partial_1}{\sqrt{3}} & \frac{\partial_2}{\sqrt{3}} & \frac{\partial_3}{\sqrt{3}} & 0 & 0 & 0 & 0 & 0 & 0 \\ -\frac{\partial_1}{\sqrt{6}} & -\frac{\partial_2}{\sqrt{6}} & \frac{2\partial_3}{\sqrt{6}} & 0 & 0 & 0 & 0 & 0 & 0 \\ -\frac{\partial_1}{\sqrt{2}} & \frac{\partial_2}{\sqrt{2}} & 0 & 0 & 0 & 0 & 0 & 0 & 0 \\ \frac{\partial_2}{\sqrt{2}} & \frac{\partial_1}{\sqrt{2}} & 0 & 0 & 0 & 0 & 0 & 0 & 0 \\ \frac{\partial_3}{\sqrt{2}} & 0 & \frac{\partial_1}{\sqrt{2}} & 0 & 0 & 0 & 0 & 0 & 0 \\ 0 & \frac{\partial_3}{\sqrt{2}} & \frac{\partial_2}{\sqrt{2}} & 0 & 0 & 0 & 0 & 0 & 0 \end{bmatrix}. \quad (\text{A-3})$$

### Gradient computation in the case of a directed force source

We compute the gradient with respect to the wavelet in the case in which the spatial component of the source is a directed force as

opposed to a moment tensor. In this case, the source terms  $m_{ij}^s$  and  $m_{ij}^a$  are zero and equation A-1 becomes

$$\begin{aligned}\frac{\partial v_i(\mathbf{x}, t)}{\partial t} &= \frac{1}{\rho(\mathbf{x})} \frac{\partial \sigma_{ij}(\mathbf{x}, t)}{\partial x_j} + \frac{1}{\rho(\mathbf{x})} f_i(\mathbf{x}) w(t), \\ \frac{\partial \sigma_{ij}(\mathbf{x}, t)}{\partial t} &= \lambda(\mathbf{x}) \frac{\partial v_k(\mathbf{x}, t)}{\partial x_k} \delta_{ij} + \mu(\mathbf{x}) \left[ \frac{\partial v_i(\mathbf{x}, t)}{\partial x_j} + \frac{\partial v_j(\mathbf{x}, t)}{\partial x_i} \right].\end{aligned}\quad (\text{A-4})$$

Here,  $f_i(\mathbf{x})$  is a known function of position and  $w(t)$  is a function of time. Rewriting equation A-4 in vector form gives

$$\frac{\partial \mathbf{u}}{\partial t} = \mathbf{A}\mathbf{u} + \mathbf{s}w, \quad (\text{A-5})$$

where  $\mathbf{A}$  and  $\mathbf{u}$  are as previously defined and

$$\mathbf{s} = (f_1, f_2, f_3, 0, 0, 0, 0, 0, 0)^T. \quad (\text{A-6})$$

In the case of a directed force source, there is no time derivative on the wavelet and so the augmented functional is now given by

$$\begin{aligned}L = J(\mathbf{u}) + \left\langle \mathbf{Tq}_1 \left| \Lambda \frac{\partial \mathbf{u}'}{\partial t} - \mathbf{A}'\mathbf{u}' - \Lambda \mathbf{Tsw} \right. \right\rangle \\ + \left\langle \mathbf{Tq}_2 \left| \mathbf{u}' - \mathbf{Tu} \right. \right\rangle.\end{aligned}\quad (\text{A-7})$$

Computing the variation of the augmented functional A-7 with respect to the wavelet  $w$  gives

$$\frac{\partial L}{\partial w} = - \int_{\mathbb{R}^3} \int_0^T \mathbf{T}^T \Lambda \mathbf{Tq}_1(\mathbf{x}, t) \cdot \mathbf{s}(\mathbf{x}) \tilde{w}(t) dt d\mathbf{x}, \quad (\text{A-8})$$

and the gradient is

$$D_w J(t) = - \int_{\mathbb{R}^3} \mathbf{T}^T \Lambda \mathbf{Tq}_1(\mathbf{x}, t) \cdot \mathbf{s}(\mathbf{x}) dx. \quad (\text{A-9})$$

In expanded form, this gradient is

$$\begin{aligned}D_w J(t) = - \int_{\mathbb{R}^3} \rho(\mathbf{x}) [f_1(\mathbf{x}) r_1(\mathbf{x}, t) + f_2(\mathbf{x}) r_2(\mathbf{x}, t) \\ + f_3(\mathbf{x}) r_3(\mathbf{x}, t)] dx,\end{aligned}\quad (\text{A-10})$$

where  $r_i$  are the adjoint velocities. In the special case of a point source given by  $f_i(\mathbf{x}) = a_i \delta(\mathbf{x} - \mathbf{x}_s)$ , equation A-10 simplifies to

$$D_w J(t) = -\rho(\mathbf{x}_s) [a_1 r_1(\mathbf{x}_s, t) + a_2 r_2(\mathbf{x}_s, t) + a_3 r_3(\mathbf{x}_s, t)]. \quad (\text{A-11})$$

Finally, the gradient of the objective functional with respect to the  $i$ th component of a directed force source in space, assuming the wavelet  $w(t)$  is known, is

$$\frac{\partial J}{\partial f_i}(\mathbf{x}) = - \int_0^T \rho(\mathbf{x}) r_i(\mathbf{x}, t) w(t) dt. \quad (\text{A-12})$$

## REFERENCES

- Artman, B., I. Podladchikov, and B. Witten, 2010, Source location using time-reverse imaging: Geophysical Prospecting, **58**, 861–873, doi: [10.1111/j.1365-2478.2010.00911.x](https://doi.org/10.1111/j.1365-2478.2010.00911.x).
- Baumstein, A., J. E. Anderson, D. L. Hinkley, and J. R. Krebs, 2009, Scaling of the objective function gradient for full waveform inversion: 79th Annual International Meeting, SEG, Expanded Abstracts, 2243–2247.
- Borisov, D., and S. C. Singh, 2015, Three-dimensional elastic full waveform inversion in a marine environment using multicomponent ocean-bottom cables: A synthetic study: Geophysical Journal International, **201**, 1215–1234, doi: [10.1093/gji/ggv048](https://doi.org/10.1093/gji/ggv048).
- Castellanos, C., V. Etienne, G. Hu, S. Operto, R. Brossier, and J. Virieux, 2011, Algorithmic and methodological developments towards full waveform inversion in 3D elastic media: 81st Annual International Meeting, SEG, Expanded Abstracts, 2793–2797.
- Douma, J., and R. Snieder, 2014, Focusing of elastic waves for microseismic imaging: Geophysical Journal International, **200**, 390–401, doi: [10.1093/gji/gju398](https://doi.org/10.1093/gji/gju398).
- Douma, J., R. Snieder, A. Fish, and P. Sava, 2013, Locating a microseismic event using deconvolution: 83rd Annual International Meeting, SEG, Expanded Abstracts, 2206–2211.
- Eisner, L., P. Duncan, W. Heigl, and W. Keller, 2009, Uncertainties in passive seismic monitoring: The Leading Edge, **28**, 648–655, doi: [10.1190/1.3148403](https://doi.org/10.1190/1.3148403).
- Eyre, T. S., and M. van der Baan, 2015, Overview of moment-tensor inversion of microseismic events: The Leading Edge, **34**, 882–888, doi: [10.1190/tle34080882.1](https://doi.org/10.1190/tle34080882.1).
- Fabien-Ouellet, G., E. Gloaguen, and B. Giroux, 2016, The adjoint state method for the viscoelastic wave equation in the velocity-stress formulation: 78th Annual International Conference and Exhibition, EAGE, Extended Abstracts, Tu SRS2 03.
- Fabien-Ouellet, G., E. Gloaguen, and B. Giroux, 2017, Time domain viscoelastic full waveform inversion: Geophysical Journal International, **209**, 1718–1734, doi: [10.1093/gji/ggx110](https://doi.org/10.1093/gji/ggx110).
- Fichtner, A., 2011, Full seismic waveform modelling and inversion: Springer, Advances in geophysical and environmental mechanics and mathematics.
- Gao, W., M. D. Sacchi, and Z. Li, 2017, Microseismic source location via elastic least squares full waveform inversion with a group sparsity constraint: 87th Annual International Meeting, SEG, Expanded Abstracts, 2814–2819.
- Gharti, H. N., V. Oye, and D. Kuhn, 2011, Simultaneous microearthquake location and moment-tensor estimation using time-reversal imaging: 81st Annual International Meeting, SEG, Expanded Abstracts, 1632–1637.
- Gunzburger, M. D., 2003, Perspectives in flow control and optimization: SIAM, Advances in design and control.
- Jarillo Michel, O., and I. Tsvankin, 2014a, Gradient calculation for waveform inversion of microseismic data in VTI media: Journal of Seismic Exploration, **23**, 201–217.
- Jarillo Michel, O., and I. Tsvankin, 2014b, Waveform inversion for parameters of microseismic sources in VTI media: 84th Annual International Meeting, SEG, Expanded Abstracts, 1045–1048.
- Kaderli, J., M. D. McChesney, and S. E. Minkoff, 2015, Microseismic event estimation in noisy data via full waveform inversion: 85th Annual International Meeting, SEG, Expanded Abstracts, 1159–1164.
- Kamei, R., and D. Lumley, 2014, Passive seismic imaging and velocity inversion using full wavefield methods: 84th Annual International Meeting, SEG, Expanded Abstracts, 2273–2277.
- Kamei, R., N. Nakata, and D. Lumley, 2015, Introduction to microseismic source mechanisms: The Leading Edge, **34**, 876–880, doi: [10.1190/tle34080876.1](https://doi.org/10.1190/tle34080876.1).
- Kim, Y., Q. Liu, and J. Tromp, 2011, Adjoint centroid-moment tensor inversions: Geophysical Journal International, **186**, 264–278, doi: [10.1111/j.1365-246X.2011.05027.x](https://doi.org/10.1111/j.1365-246X.2011.05027.x).
- Levander, A., 1988, Fourth-order finite-difference P-SV seismograms: Geophysics, **53**, 1425–1436, doi: [10.1190/1.1442422](https://doi.org/10.1190/1.1442422).
- Madariaga, R., 1976, Dynamics of an expanding circular fault: Bulletin of the Seismological Society of America, **66**, 639–666.
- Maxwell, S., 2014, Microseismic imaging of hydraulic fracturing: Improved engineering of unconventional shale reservoirs: SEG, Distinguished instructor series.
- Maxwell, S. C., D. Chorney, and S. D. Goodfellow, 2015, Microseismic geo-mechanics of hydraulic-fracture networks: Insights into mechanisms of

- microseismic sources: The Leading Edge, **34**, 904–910, doi: [10.1190/tle34080904.1](https://doi.org/10.1190/tle34080904.1).
- McChesney, M. D., S. E. Minkoff, and G. A. McMechan, 2016, Rate and state flow and deformation simulation of microseismicity with elastic emission wavefield synthesis: 86th Annual International Meeting, SEG, Expanded Abstracts, 5055–5059.
- McClure, M. W., and R. N. Horne, 2011, Investigation of injection-induced seismicity using a coupled fluid flow and rate/state friction model: *Geophysics*, **76**, no. 2, WC181–WC198, doi: [10.1190/geo2011-0064.1](https://doi.org/10.1190/geo2011-0064.1).
- Métivier, L., R. Brossier, S. Operto, and J. Virieux, 2017, Full waveform inversion and the truncated Newton method: *SIAM Review*, **59**, 153–195, doi: [10.1137/16M1093239](https://doi.org/10.1137/16M1093239).
- Minkoff, S., and W. Symes, 1997, Full waveform inversion of marine reflection data in the plane wave domain: *Geophysics*, **62**, 540–553, doi: [10.1190/1.1444164](https://doi.org/10.1190/1.1444164).
- Minkoff, S. E., 2002, Spatial parallelism of a 3D finite difference velocity-stress elastic wave propagation code: *SIAM Journal on Scientific Computing*, **24**, 1–19, doi: [10.1137/S1064827501390960](https://doi.org/10.1137/S1064827501390960).
- Morency, C., and R. J. Mellors, 2012, Full moment tensor and source location inversion based on full waveform adjoint inversion: Application at the Geysers geothermal field: 82nd Annual International Meeting, SEG, Expanded Abstracts, doi: [10.1190/segam2012-0869.1](https://doi.org/10.1190/segam2012-0869.1).
- Oberai, A., N. Gockhale, and G. Feijoo, 2003, Solution of inverse problems in elasticity imaging using the adjoint method: *Inverse Problems*, **19**, 297–313, doi: [10.1088/0266-5611/19/2/304](https://doi.org/10.1088/0266-5611/19/2/304).
- Oye, V., and M. Roth, 2003, Automated seismic event location for hydrocarbon reservoirs: *Computers and Geosciences*, **29**, 851–863, doi: [10.1016/S0098-3004\(03\)00088-8](https://doi.org/10.1016/S0098-3004(03)00088-8).
- Plessix, R., 2006, A review of the adjoint-state method for computing the gradient of a functional with geophysical applications: *Geophysical Journal International*, **167**, 495–503, doi: [10.1111/j.1365-246X.2006.02978.x](https://doi.org/10.1111/j.1365-246X.2006.02978.x).
- Ramos-Martinez, J., and G. A. McMechan, 2001, Source-parameter estimation by full wave form inversion in 3D heterogeneous, viscoelastic, anisotropic media: *Bulletin of the Seismological Society of America*, **91**, 276–291, doi: [10.1785/0120000017](https://doi.org/10.1785/0120000017).
- Rutledge, J. T., and W. S. Phillips, 2003, Hydraulic stimulation of natural fractures as revealed by induced microearthquakes, Carthage Cotton Valley gas field, east Texas: *Geophysics*, **68**, 441–452, doi: [10.1190/1.1567214](https://doi.org/10.1190/1.1567214).
- Sharan, S., R. Wang, T. van Leeuwen, and F. J. Herrmann, 2016, Sparsity-promoting joint microseismic source collocation and source-time function: 86th Annual International Meeting, SEG, Expanded Abstracts, 2574–2579.
- Sjögren, B., and N. A. Petersson, 2014, Source estimation by full waveform inversion: *Journal of Scientific Computing*, **59**, 247–276, doi: [10.1007/s10915-013-9760-6](https://doi.org/10.1007/s10915-013-9760-6).
- Sleefe, G., D. Aldridge, G. Elbring, J. Claassen, H. Garbin, and R. Shear, 1998, Advanced subterranean warfare (ASW) for deep underground structures: Technical Report SAND98-0988, Sandia National Labs.
- Trojanowski, J., and L. Eisner, 2017, Comparison of migration-based location and detection methods for microseismic events: *Geophysical Prospecting*, **65**, 47–63, doi: [10.1111/1365-2478.12366](https://doi.org/10.1111/1365-2478.12366).
- Vavryčuk, V., and D. Kühn, 2012, Moment tensor inversion of waveforms: A two-step time-frequency approach: *Geophysical Journal International*, **190**, 1761–1776, doi: [10.1111/j.1365-246X.2012.05592.x](https://doi.org/10.1111/j.1365-246X.2012.05592.x).
- Vigh, D., K. Jiao, D. Watts, and D. Sun, 2014, Elastic full-waveform inversion application using multicomponent measurements of seismic data collection: *Geophysics*, **79**, no. 2, R63–R77, doi: [10.1190/geo2013-005.1](https://doi.org/10.1190/geo2013-005.1).
- Virieux, J., 1984, SH-wave propagation in heterogeneous media: Velocity-stress finite difference method: *Geophysics*, **49**, 1933–1942, doi: [10.1190/1.1441605](https://doi.org/10.1190/1.1441605).
- Virieux, J., 1986, P-SV wave propagation in heterogeneous media: Velocity-stress finite-difference method: *Geophysics*, **51**, 889–901, doi: [10.1190/1.442147](https://doi.org/10.1190/1.442147).
- Virieux, J., and S. Operto, 2009, An overview of full-waveform inversion in exploration geophysics: *Geophysics*, **74**, no. 6, WCC1–WCC26, doi: [10.1190/1.3238367](https://doi.org/10.1190/1.3238367).
- Wang, J., H. Zhou, Y. Tian, and H. Zhang, 2012, A new scheme for elastic full waveform inversion based on velocity-stress wave equations in time domain: 82nd Annual International Meeting, SEG, Expanded Abstracts, doi: [10.1190/segam2012-0561.1](https://doi.org/10.1190/segam2012-0561.1).
- Wu, Y., and G. A. McMechan, 1996, Elastic full-waveform inversion for earthquake source parameters: *Geophysical Journal International*, **127**, 61–74, doi: [10.1111/j.1365-246X.1996.tb01535.x](https://doi.org/10.1111/j.1365-246X.1996.tb01535.x).
- Yao, Z., and G. F. Margrave, 2000, Elastic wavefield modelling in 3D by fourth-order staggered-grid finite difference technique: CREWES Research Report, **12**, 1–10.
- Zhang, X., W. Zhang, and J. Zhang, 2014, Elastic full waveform inversion of microseismic data for location and source mechanism: 84th Annual International Meeting, SEG, Expanded Abstracts, 2256–2260.
- Zhebel, O., and L. Eisner, 2015, Simultaneous microseismic event localization and source mechanism determination: *Geophysics*, **80**, no. 1, KS1–KS9, doi: [10.1190/geo2014-0055.1](https://doi.org/10.1190/geo2014-0055.1).